

Multiferroicity in doped hexagonal LuFeO₃

Steven M. Disseler,¹ Xuan Luo,² Bin Gao,³ Yoon Seok Oh,^{3,4} Rongwei Hu,³ Yazhong Wang,³ Dylan Quintana,⁵
 Alexander Zhang,^{1,*} Qingzhen Huang,¹ June Lau,⁶ Rick Paul,¹ Jeffrey W. Lynn,¹
 Sang-Wook Cheong,^{2,3} and William Ratcliff II¹

¹*NIST Center for Neutron Research, National Institute of Standards and Technology, Gaithersburg, Maryland 20899, USA*

²*Laboratory for Pohang Emergent Materials and Max Plank POSTECH Center for Complex Phase Materials, Pohang University of Science and Technology, Pohang 790-784, Korea*

³*Rutgers Center for Emergent Materials and Department of Physics and Astronomy, Rutgers University, Piscataway, New Jersey 08854, USA*

⁴*Department of Physics, Ulsan National Institute of Science and Technology (UNIST), Ulsan 689-798, Korea*

⁵*Carnegie Mellon University, Pittsburgh, Pennsylvania 15213, USA*

⁶*National Institute of Standards and Technology, Gaithersburg, Maryland 20899, USA*

(Received 22 May 2015; published 27 August 2015)

The hexagonal phase of LuFeO₃ is a rare example of a multiferroic material possessing a weak ferromagnetic moment, which is predicted to be switchable by an electric field. We stabilize this structure in bulk form through Mn and Sc doping, and determine the complete magnetic and crystallographic structures using neutron-scattering and magnetometry techniques. The ferroelectric $P6_3cm$ space group is found to be stable over a wide concentration range, ordering antiferromagnetically with Néel temperatures that smoothly increase following the ratio of c to a (c/a) lattice parameters up to 172 K, the highest found in this class of materials to date. The magnetic structure for a range of temperatures and dopings is consistent with recent studies of high quality epitaxial films of pure hexagonal LuFeO₃ including a ferromagnetic moment parallel to the ferroelectric axis. We propose a mechanism by which room-temperature multiferroicity could be achieved in this class of materials.

DOI: [10.1103/PhysRevB.92.054435](https://doi.org/10.1103/PhysRevB.92.054435)

PACS number(s): 75.25.-j, 75.85.+t, 75.30.-m

I. INTRODUCTION

Materials exhibiting simultaneous ferroelectric and magnetic ordering, known as multiferroics, are extraordinarily rare in nature but have the potential for tremendous impact for electronic and magnetic devices including magnetoresistive random access memory (MRAM), low-power microwave devices, and other spin-based electronics [1–5]. The scarcity of such materials stems from the almost mutually exclusive origin of the two orders: magnetism requires partially unfilled d or f electron orbitals, while ferroelectric distortions occur primarily through hybridization with completely empty d shells [3]. Furthermore, the requirement that the crystalline structure has a noncentrosymmetric space group to support ferroelectricity places further restrictions on possible material candidates [6]. Even in those rare cases where both orders exist [7], useful systems require significant magnetoelectric coupling between ferroelectric and magnetic moments that is often found to be quite weak or is significant only at cryogenic temperatures [4]. As such, discovery of new materials, or mechanisms to improve the magnetoelectric properties of known multiferroics, is of upmost importance if such devices are to exist in the future.

The hexagonal manganites $RMnO_3$ ($R = \text{La-Lu, Y, etc.}$) are a well-studied multiferroic system, with ferroelectric order developing well above room temperature—above $T_c \sim 1000$ K in some cases—resulting from a $\sqrt{3} \times \sqrt{3}$ or trimerization-type crystalline distortion into the noncentrosymmetric $P6_3cm$ polar structure [8–10] shown in Fig. 1(a). Despite the presence of strong antiferromagnetic interactions the geometrical

frustration inherent in the triangular lattice formed by the Mn spins [Figs. 1(c)–1(f)] hinders the formation of long-range magnetic order to below 100 K in most cases [8,11]. Recent *ab initio* calculations [12] have suggested that the closely related family of hexagonal ferrites such as LuFeO₃ (h -LFO) may exhibit greatly enhanced magnetic properties relative to their manganite counterparts due to enhanced exchange interactions, larger localized magnetic moments, and differences in the local electronic anisotropy between Mn³⁺ and Fe³⁺. In fact, recent investigations of thin films of h -LFO demonstrate that magnetic order occurs as high as 150 K with the simultaneous appearance of a net ferromagnetic (FM) moment parallel to the ferroelectric axis [13–16] consistent with *ab initio* calculations [12]. To date, studies of this material have been limited to thin films as h -LuFeO₃ is metastable in bulk and instead forms the centrosymmetric and nonpolar orthorhombic $Pbnm$ structure, precluding ferroelectricity [17]. In order to study details of the crystal structure as well as the spin dynamics to determine the magnetic exchange interactions and anisotropy, bulk samples are required.

For this work we successfully synthesized and characterized bulk h -LuFeO₃ by substitution into either the Lu site using Sc or into the Fe site using Mn. We find that the structure is stable and single phase even up to 75% Fe and for ~50% Sc doping, retaining the correct space-group symmetry as shown in a previous study [18]. Using detailed neutron-scattering and magnetometry techniques we find that both routes maintain the high-temperature ferroelectric properties observed in LuMnO₃ while simultaneously improving the magnetic and magnetoelectric properties toward that theorized for pure h -LuFeO₃. This includes the highest T_N observed to date for this class of materials (172 K), and the appearance of weak ferromagnetism consistent with thin-film studies. Furthermore, we are able to construct a phase diagram

* Also at Montgomery Blair High School, Silver Spring, MD 20901, USA.

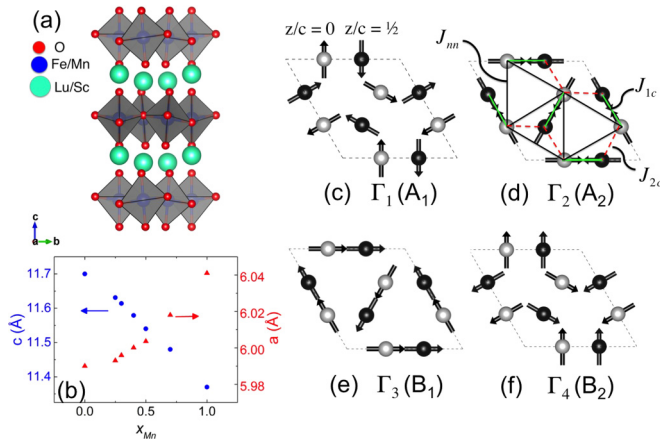


FIG. 1. (Color online) (a) $P6_3cm$ crystal structure as determined from x-ray and neutron powder-diffraction refinement. (b) Lattice parameters vs Mn concentration, smoothly interpolating between those of pure LuMnO_3 [8,19–23] and epitaxially grown h - LuFeO_3 thin films [15,16] following Vegard’s law. (c)–(e) Potential magnetic structures of h -LFO. The Γ_i ’s correspond to the one-dimensional irreducible representations while labels in parentheses correspond to the notation used in Ref. [6]. The exchange interactions J_{mn} and J_c are shown in (d).

describing the structural origin for improvement of magnetism and magnetic order and suggest mechanisms for reaching room-temperature magnetoelectricity in this class of materials.

II. EXPERIMENT

Polycrystalline samples of Mn-doped LuFeO_3 were synthesized by the solid-state reaction method. Stoichiometric amounts of Lu_2O_3 , Fe_2O_3 , and MnO_2 (purity > 99.9%) were mixed thoroughly, pressed into pellets, and sintered at 1400 °C in air for 100 h with intermediate grinding to ensure a complete reaction and sample homogeneity. Platelike single crystals of Mn-doped LuFeO_3 with masses up to 10 mg were grown using Bi_2O_3 flux in a Pt crucible. A mixture of polycrystalline $\text{LuFe}_{1-x}\text{Mn}_x\text{O}_3$ and Bi_2O_3 in a ratio of 1:6 was held at 1300 °C for 10 h and slowly cooled down to 950 °C at 3 °C/h. The furnace was then turned off and single crystals were mechanically separated out from the flux. A Sc-doped LuFeO_3 single crystal was grown under 0.8-MPa O_2 atmosphere using an optical floating zone furnace. The feed rod material was prepared by a similar solid-state reaction procedure. The as-grown crystal rod was then annealed under 20 MPa O_2 pressure at 950 °C in a high-pressure oxygen furnace to release thermal stress. The final compositions of single crystals were verified using energy dispersive x-ray spectroscopy at several positions and example crystals and by prompt γ -ray activation analysis using cold neutrons at the NIST Center for Neutron Research.

The magnetic susceptibility was measured between 2 and 400 K under zero-field-cooled (ZFC) or field-cooled (FC) conditions in a field of 0.1 T. Electric polarization loop measurements were performed at room temperature on a single crystal of Sc-doped LuFeO_3 polished to a thickness of 18 μm using an excitation frequency of 256 Hz.

Powder diffraction and inelastic neutron scattering were performed at the NIST Center for Neutron Research. High-

resolution powder-diffraction patterns were taken on the BT-1 powder diffractometer using a $\text{Cu}(311)$ monochromator for neutrons of wavelength $\lambda = 1.540 \text{ \AA}$ or a $\text{Ge}(311)$ monochromator with $\lambda = 2.0775 \text{ \AA}$, and collimations of $60' - 25' - 7'$, and were refined using the FULLPROF software package [19]. Two-axis diffraction measurements on the BT-7 triple axis spectrometer [20] were performed using the position sensitive detector (PSD) with initial energy $E_i = 14.7 \text{ meV}$ ($\lambda = 2.359 \text{ \AA}$) with pyrolytic graphite (PG) monochromator and filters which were placed before and after the sample, and horizontal collimations with full width at half maximum of open- $80' - S - 80' - \text{radial}$ PSD. Inelastic measurements on the BT-7 triple axis spectrometer were made in traditional three-axis mode with fixed final energy $E_f = 14.7 \text{ meV}$, PG monochromator and analyzer, and collimations of open- $80' - S - 80' - 120'$ with the analyzer under horizontally focused condition. Diffraction measurements of single crystals were performed on the BT-4 triple axis spectrometer with collimation settings of $40' - 40' - S - 40' - 120'$ and E_f of either 14.7 or 35 meV. Measurements on the SPINS triple axis spectrometer were made with guide- $80' - S - 80' - 120'$ collimation and $E_f = 3.7 \text{ meV}$ with a cooled BeO filter. Powders with masses between 5 and 11 g were sealed in an Al canister with helium exchange gas and were cooled to 5 K in a closed-cycle refrigerator. Single crystals were mounted onto a silicon wafer using fluorinated grease and then sealed in an Al canister with helium exchange gas.

III. RESULTS AND DISCUSSION

A. $\text{LuFe}_{1-x}\text{Mn}_x\text{O}_3$

Polycrystalline and single crystal samples of $\text{LuFe}_{1-x}\text{Mn}_x\text{O}_3$ with $x_{Mn} \geq 0.25$ are found to be single phase and homogeneous at room temperature by x-ray diffraction. All reflections could be indexed to the noncentrosymmetric hexagonal $P6_3cm$ space group. Both a and c lattice parameters are found to vary linearly as a function of x_{Mn} as shown in Fig. 1(b), smoothly interpolating between those of pure LuMnO_3 [8,21–23] and epitaxially grown h - LuFeO_3 thin films [15,16] following Vegard’s law. The temperature-dependent magnetic susceptibility ($\chi_{dc} = M/H$) is found to vary greatly with Mn concentration, as shown in Figs. 2(a)–2(d). A sharp upturn in the powder-averaged susceptibility is observed at $T_N \sim 134 \text{ K}$ in the $x_{Mn} = 0.25$ sample with a residual ferromagnetic moment and strong dependence on magnetic field cooling history. The susceptibility of a single crystal with $x_{Mn} = 0.33$ is measured with $H \parallel c$ [Fig. 2(b)], where a similar bifurcation is observed, indicating weak or canted ferromagnetism along the c axis as is found in pure h - LuFeO_3 films. Interestingly, a maximum in the susceptibility is observed near 100 K even for high Fe concentrations indicating that the ferromagnetic moment does not simply saturate below T_N . With increasing Mn concentration the susceptibility shows a reduced dependence on the cooling history until no ferromagnetic moment is observed for $x_{Mn} = 0.5$ [Fig. 2(d)] indicative of a purely antiferromagnetic ground state similar to that of LuMnO_3 [23,24]. The negative ZFC susceptibility observed for samples below T_N is indicative of the weak ferromagnetism from an unquenched applied

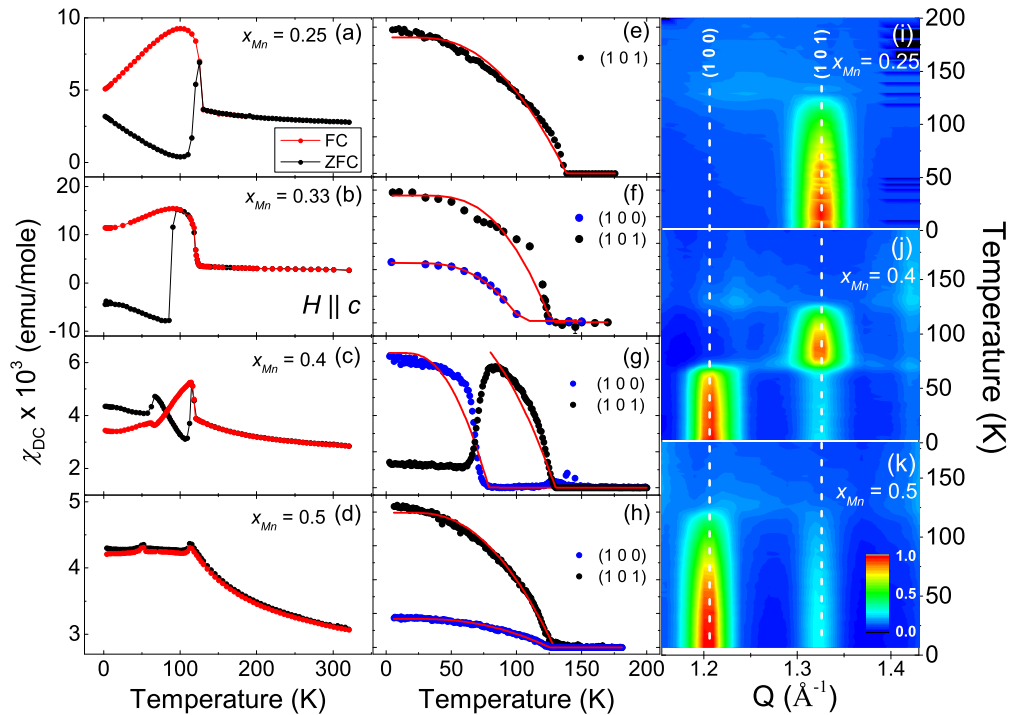


FIG. 2. (Color online) (a)–(d) Magnetic susceptibility of the four- x_{Mn} concentrations, as indicated. (a) (c), and (d) are powder averaged while (b) is for a field applied parallel to the c axis for a 10-mg single crystal ($1 \text{ emu/mol} = 4\pi \times 10^{-6} \text{ m}^3/\text{mol}$). (e)–(h) Integrated neutron-diffraction intensities of the magnetic (100) and/or (101) reflections as a function of temperature for $x_{\text{Mn}} = 0.25, 0.33, 0.4,$ and 0.5 respectively. Solid lines represent fitted mean-field order parameters. (i)–(k) Temperature dependence of the total neutron scattering as measured with the position sensitive detector normalized to maximum intensity in each respective panel. The locations of the (100) and (101) magnetic reflections are indicated for clarity by the dashed line and comparison with (e)–(h).

magnetic field, however, may also stem from the pinning of canted spins, particularly near domain walls [25].

For all samples, χ_{dc} above 200 K follows a Curie-Weiss behavior; linear fits of the inverse susceptibility between 200 and 350 K (not shown) give negative Curie-Weiss temperatures that decrease in magnitude from $\theta_{\text{CW}} = -950(10)$ K for $x_{\text{Mn}} = 0.25$ to $\theta_{\text{CW}} = -800(10)$ K for $x_{\text{Mn}} = 0.5$, comparable to $\theta_{\text{CW}} \sim -800$ K found for LuMnO₃ [23,24]. The effective paramagnetic moment is between 5.2 and $5.4 \mu_{\text{B}}/\text{ion}$, quite close to the 5.4 to $5.7 \mu_{\text{B}}/\text{ion}$ expected for a simple combination of $S = 2 \text{ Mn}^{3+}$ and $S = 5/2 \text{ Fe}^{3+}$ species.

The onset of antiferromagnetic order is directly determined from neutron diffraction. At 5 K we find diffraction peaks corresponding to structurally forbidden (100) and (101) reflections, with no noninteger reflections indicating that the magnetic unit cell is the same as the crystalline one. In the case of polycrystalline samples, a range of scattering angles covering both (100) and (101) reflections could be measured simultaneously using a position sensitive detector (PSD) as shown in Figs. 2(i)–2(k). Fitting the integrated intensity of the (101) with a simple mean-field order parameter function, shown as the solid curves in Figs. 2(e)–2(h), we determine $T_N = 134(1)$ K, $127(1)$ K, $125(1)$ K, and $124(1)$ K for $x_{\text{Mn}} = 0.25, 0.33, 0.4,$ and 0.5 , respectively. For the intermediate concentrations ($x_{\text{Mn}} = 0.33$ and 0.4) the (100) and (101) intensities have very different onset temperatures, indicating that there is a spin-reorientation transition that occurs below the initial magnetic ordering. Performing a similar fit of the (100) reflection results in a spin-reorientation transition $T_R = 107$ K

and 50 K for $x = 0.33$ and 0.4 samples, respectively. The nature of the ground state and spin reorientation can be understood from representational analysis of the $P6_3cm$ crystallographic space group [26,27]. The result is four one-dimensional representations describing different 120° -type magnetic structures in each plane as shown in Figs. 1(c)–1(f), labeled using recent convention [11]. The A_1 and B_1 structures cannot be distinguished from one another in unpolarized neutron diffraction, nor can the A_2 structure be distinguished from the B_2 one, resulting in pairs of homomorphic representations. The (100) reflection, however, is only allowed for the A_1 and B_1 representations, thereby allowing homomorphic pairs to be distinguished from one another without the need for polarized neutron scattering [26,27]. Furthermore, only the A_2 representation allows for a ferromagnetic moment along the c axis; all other structures either do not allow canting or only allow antiferromagnetic alignment between layers resulting in no net moment along the c direction. The $x_{\text{Mn}} = 0.25$ sample must therefore be purely in the A_2 phase as no (100) reflection is present, while signs of ferromagnetism do appear below T_N . All other samples exhibit some combination of these characteristics and are thus at best an admixture of the A_2 phase and either the A_1 or B_1 phases.

The detailed magnetic structures for each sample may be solved through refinement of the neutron powder-diffraction patterns, as shown in Fig. 3 for data taken with neutrons having a wavelength $\lambda = 1.540 \text{ \AA}$. For $x_{\text{Mn}} = 0.25$ we find that the A_2 model sufficiently describes the magnetic structure as expected, where the refined average magnetic moment on

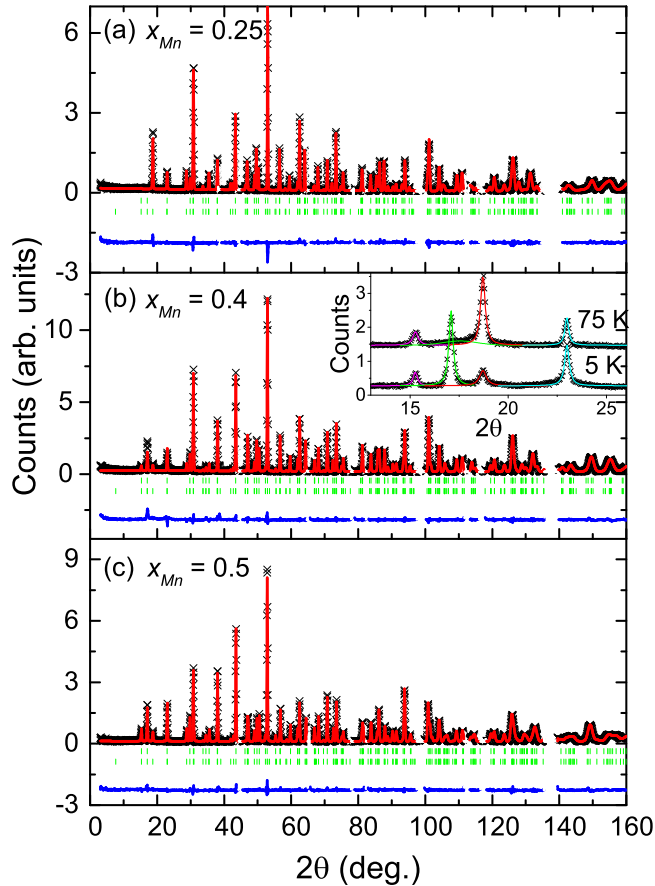


FIG. 3. (Color online) Refinement of neutron powder-diffraction patterns, (a) $x_{\text{Mn}} = 0.25$, (b) $x_{\text{Mn}} = 0.4$, and (c) $x_{\text{Mn}} = 0.5$ at 5 K with $\lambda = 1.540 \text{ \AA}$ neutrons taken at 5 K. The refinement (solid curve) is in excellent agreement with the data (\times) as shown by small deviations in the lower difference curve (blue) at nuclear and magnetic Bragg peaks at the vertical bars (\updownarrow) for all but the low-angle portion of $x = 0.4$. Regions with scattering from the Al canister have been removed. (b) Inset: Low angle diffraction of $x_{\text{Mn}} = 0.4$ taken at 75 and 5 K fitted with a series of Lorentzian peaks color coded to each reflection with (002) (orange), (100) (green), (101) (red), and (102) (blue).

the transition metal site is $m = 3.62(3) \mu_{\text{B}}/\text{ion}$. Similarly, the ground state of the $x = 0.5$ sample could also be refined with a single representation, but using either A_1 [Fig. 1(c)] or B_1 [Fig. 1(e)]. A smaller magnetic moment is also observed for this concentration, with $m = 3.45(5) \mu_{\text{B}}/\text{ion}$. The magnetic structure of the $x_{\text{Mn}} = 0.33$ single crystal was refined from a series of rocking curves of magnetic and nuclear reflections in the $H0L$ scattering zone [29]. As both (100) and (101) reflections were observed at low temperature, the resolution-corrected integrated intensities were refined using a two-representation model with basis vectors of both the A_1 and A_2 representations, thereby allowing for rotation of the moments in the plane while requiring only two free parameters after scaling to the integrated intensities of several nuclear reflections. At 5 K the moments are found to be coherently rotated in the a - b plane $25(5)^\circ$ from the pure A_2 configuration toward the A_1 with $m = 3.55(9) \mu_{\text{B}}$, intermediate between the $x_{\text{Mn}} = 0.25$ and 0.5 compositions. It should be noted that the small ferromagnetic component of the moment observed in

magnetic susceptibility [Figs. 2(a)–2(c)] could not be determined here and was thus fixed to zero in these refinements; this is consistent with a ferromagnetic moment less than $0.1 \mu_{\text{B}}/\text{Fe}$ based upon recent studies of thin films [13–16], whose intensity is further suppressed by the structure factor for the special position of the transition metal species.

Unlike the $x_{\text{Mn}} = 0.25$ and 0.5 compositions, no adequate refinement could be made for the $x_{\text{Mn}} = 0.4$ composition using any single representation or simple general combination thereof despite an excellent fit of the crystalline structure [28]. This is due to the existence of both broad and sharp peaks as shown in the inset of Fig. 3(b), implying the coexistence of short- and long-range-ordered regions of nonhomomorphic structures. The low angle portion of the diffraction pattern taken above and below T_R is best described by a series of Lorentzian peaks, the half width at half maximum giving the approximate size of each ordered region. At 75 K ($T_N > T > T_R$) there is a coexistence of the A_1/B_1 and A_2 phases, the majority being A_2 given by intense narrow peaks at the (101) reflection, with the regions of A_1/B_1 shown by a broad peak centered at (100) giving an average dimension $\sim 40 \text{ \AA}$, or roughly seven unit cells along the a or b directions or four unit cells along c . At 5 K the reverse is true, and we find much smaller regions of A_2 , no larger than $\sim 20 \text{ \AA}$, within the majority A_1/B_1 matrix. The coexistence of two representations is inconsistent with a purely second-order transition according to Landau phenomenology [29], instead indicating a weakly first-order transition for this concentration. Calculations of the ground-state energy for each representation have shown that there is only a very small difference between homomorphic representations ($< 0.05 \text{ meV/ion}$) [12], thus it is quite reasonable to expect that subtle variations induced by alloying would affect the selection of the ground state as we have observed.

Regardless of the ground-state configuration, the magnitude of the ordered moment decreases with x_{Mn} as expected for a linear combination of larger (Fe) and smaller (Mn) moments. Interestingly, these are substantially reduced from the values determined through our Curie-Weiss analysis by over $1 \mu_{\text{B}}/\text{ion}$. This phenomenon has been observed in many isostructural RMnO_3 compounds [11,21–27] and therefore cannot be the result of orbital fluctuations or other processes which would strongly depend on occupancy of the d_{2z} orbital. This instead suggests that fast fluctuations continue to exist even in the Néel state as a consequence of the underlying geometrically frustrated lattice and near degeneracy of distinct spin configurations. Further evidence for frustration is apparent in measurements of the diffuse scattering above T_N as shown in Figs. 2(i)–2(k), where the diffuse contributions between $Q = 1.1$ and 1.5 \AA^{-1} are indicative of cooperative paramagnetic fluctuations ascribed to the rotational freedom in the a - b plane, similar to YMnO_3 [28].

B. $\text{Lu}_{0.5}\text{Sc}_{0.5}\text{FeO}_3$

It has been shown previously that substitution of the smaller-radii Sc ion onto the Lu site may also stabilize the hexagonal form of $\text{Lu}_{1-y}\text{Sc}_y\text{FeO}_3$ near $y \sim 0.5$ [18]; such compounds may allow a simpler description of hexagonal ferrite systems in bulk due to the presence of only one type of magnetic ion compared with the Fe-Mn alloyed system. One

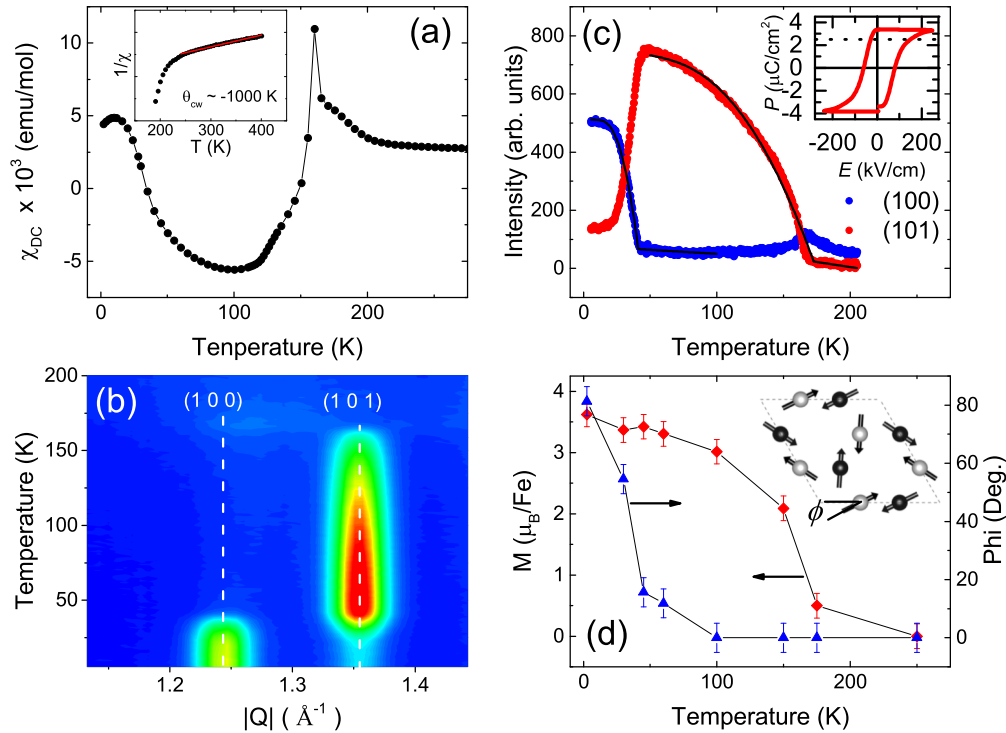


FIG. 4. (Color online) Magnetic order in Lu_{0.5}Sc_{0.5}FeO₃ (a) magnetic susceptibility after zero-field cooling with inverse susceptibility shown in the inset. (b) Intensity map of the neutron-diffraction intensity about the magnetic (100) and (101) reflections, (c) integrated intensity of each reflection with mean-field order-parameter fits shown as the solid curves. Inset: Electric polarization as function of applied electric field at room temperature for a thin polished crystal; the value calculated from structural refinement is shown by a dashed line. (d) Magnetic moment and rotation angle from refinement of powder-diffraction patterns. Error bars represent one standard deviation. Inset: Schematic of the $A_1 + A_2$ magnetic structure defining the angle ϕ .

12-g polycrystalline sample was fabricated with $y = 0.5$ and investigated using similar magnetometry, neutron diffraction, and neutron spectroscopy techniques in order to compare with the mixed transitionmetal ion Fe-Mn series. Shown in Fig. 4(a), a transition in the zero-field (ZF) magnetic susceptibility occurs near 175 K, while well above Curie-Weiss behavior is observed (inset); a paramagnetic moment of $5.5\mu_B/\text{Fe}$ and $\theta_{\text{CW}} \sim -1000$ K are extracted from a linear fit of the inverse susceptibility, both of which are somewhat larger relative to that determined for $x_{\text{Mn}} = 0.25$. The intensities of the (100) and (101) magnetic reflections are shown in Figs. 4(b) and 4(c), where we observe a sharp onset of the (101) at $T_N = 172(1)$ K, followed by a spin-reorientation transition at $T_R = 45(1)$ K as indicated by the sharp drop in intensity at the (101) and onset of the (100) reflection. The magnetic and crystallographic structures are determined as a function of temperature using neutron powder diffraction with neutrons having a wavelength of 2.0775 \AA and $\lambda = 1.540 \text{ \AA}$ respectively [29]. The magnetic structure was refined using the two-representation ($A_1 + A_2$) model shown in Fig. 4(d) for all temperatures in order to determine both the magnitude of the ordered moment as well as a common rotation angle ϕ in the $hk0$ plane. We find that the A_2 structure ($\phi = 0$) exists over the temperature range $T_N > T > T_R$, while the ground-state structure can be described entirely of the A_1 type ($\phi = 90^\circ$). Unlike for Mn doping where both short-range and long-range-ordered phases exist at low temperatures, only long-range order exists in Lu_{0.5}Sc_{0.5}FeO₃ as no broadening of the magnetic reflections is observed well

below T_N . Furthermore, as shown in Fig. 4(d), the magnetic moment appears to saturate above T_R indicating that the transition at T_R is a coherent rotation of the moments in the plane rather than a nucleation of distinct magnetic representations. The refined moment at 5 K is substantially reduced relative to the paramagnetic one, with $m = 3.5(1)\mu_B/\text{Fe}$ again indicative of fast fluctuations observed in Mn-containing samples.

Similar spin reorientations have been observed in the isostructural RMnO₃ series, where the ground-state spin configuration strongly depends upon the displacement of the average transition metal position from the ideal $x/a = 1/3$ position [30]. When $x/a = 1/3$ the Mn lattice forms a perfect triangular lattice such that all nearest-neighbor intraplane superexchange interactions are equal resulting in a completely frustrated structure. In this case the two most prominent super-superexchange pathways providing interplane couplings are also equal such that $J_{1c} = J_{2c}$ [Fig. 1(d)], effectively decoupling the individual two-dimensional layers. Displacement of the Fe/Mn ions by a small amount lowers the energy of either A -type or B -type representation by a corresponding amount $\Delta J_c = J_{1c} - J_{2c}$ depending upon if $x/a > 1/3$ or $x/a < 1/3$, respectively [30,31]. From refinement of the neutron-diffraction patterns we find that for $x_{\text{Mn}} = 0.25$, $x/a = 0.3347(1)$, consistent with the AFM interplane interaction needed for the A_2 representation. For $x_{\text{Mn}} = 0.5$ we find that $x/a = 0.3325(10)$, leading to ferromagnetic interplane coupling consistent with the B_1 rather than the A_1 ground state. In the case of the $x_{\text{Mn}} = 0.4$ compound, x/a is

TABLE I. Amplitude of the K_1 , K_3 , and Γ_{2-} phonon modes derived for the $P6_3/mmc \rightarrow P6_3cm$ distortion determined from the refined atomic positions at 5 K. Data for $x_{\text{Mn}} = 1$ are taken from Ref. [19]. The values in the table are given in units of Å. The ferroelectric polarization calculated using the refined atomic positions is given for comparison with that measured for $\text{Lu}_{0.5}\text{Sc}_{0.5}\text{FeO}_3$.

x_{Mn}	K_1	K_3	Γ_{2-}	P ($\mu\text{C}/\text{cm}^2$)
0.25	0.0223	1.0115	0.1598	3.4(1)
0.4 (5 K)	0.0228	1.0064	0.1914	2.2(1)
0.4 (75 K)	0.0052	1.0091	0.2026	2.1(1)
0.5	0.0238	1.0127	0.2341	1.9(1)
1	0.0732	1.032	0.2052	1.9(1)
$\text{Lu}_{0.5}\text{Sc}_{0.5}\text{FeO}_3$	0.0541	0.8384	0.3785	2.3(1) (calc.) 3.34(5) (meas.)

found to shift between these two conditions at T_R such that $x/a = 0.3349(10)$ for $T_N > T > T_R$ and $x/a = 0.3318(10)$ for $T < T_R$. In $\text{Lu}_{0.5}\text{Sc}_{0.5}\text{FeO}_3$, $x/a = 0.3345(10)$ below T_R indicating the ground state is A_1 type, but the temperature dependence is nonmonotonic, dropping below 1/3 only over the range $T_N > T > T_R$ [28].

A more general method of describing the displacements of the various atomic positions is in terms of the amplitude of the K_1 , K_3 , and Γ_{2-} phonon modes that condense during the distortion from the high-temperature nonpolar $P6_3/mmc$ structure to the polar $P6_3cm$ structure [9,12]. K_1 and K_3 are zone-boundary modes stemming from $q = (1/3, 1/3, 0)$. The K_1 mode describes distortions of the apical oxygen and transition metal in the a - b plane, while the K_3 mode corresponds to the rotation of the oxygen trigonal bipyramids (hexahedra) and buckling of the Lu-O planes leading to the $\sqrt{3} \times \sqrt{3}$ distortion [9,31]. As neither mode produces a net polar moment, ferroelectricity can only be generated via coupling of the K_3 to the Γ_{2-} mode at the zone center [9]. The magnitude of each mode is determined with the AMPLIMODES software [32] for each of the samples based on the atomic positions at 5 K refined from powder neutron diffraction [28], resulting in the displacement amplitudes listed in Table I.

We find that the amplitude of the K_1 mode at 5 K increases monotonically with x_{Mn} while K_3 and Γ_{2-} do not. Furthermore, for the case of $x = 0.4$ we find a large increase in K_1 as the system is cooled though T_R , while K_3 and Γ_{2-} do not show a significant change at this temperature. Taken together these results indicate that the K_1 mode plays an important role in the spin-reorientation transition and determination of the ground-state magnetic structure as suggested from recent *ab initio* calculations [31]. On the other hand, this does not appear to play a pivotal role in determining the ordering temperature as the amplitude of the K_1 mode for $\text{Lu}_{0.5}\text{Sc}_{0.5}\text{FeO}_3$ is between that determined for LuMnO_3 and $\text{LuFe}_{0.75}\text{Mn}_{0.25}\text{O}_3$, yet has a higher magnetic ordering temperature than both compounds.

The spontaneous ferroelectric polarization in the multiferroic phase at low temperature is calculated from the atomic displacements relative to their respective positions in the undistorted $P6_3/mmc$ paraelectric phase. Shown in Table I, the calculated values range between 1.9 and $3.4 \mu\text{C}/\text{cm}^2$ for $\text{LuFe}_{1-x_{\text{Mn}}}\text{Mn}_{x_{\text{Mn}}}\text{O}_3$ and $2.3 \mu\text{C}/\text{cm}^2$ for $\text{Lu}_{0.5}\text{Sc}_{0.5}\text{FeO}_3$. These values are comparable with those observed in hexagonal

manganites such as YMnO_3 [10]. The ferroelectric polarization was also experimentally determined at room temperature as a function of electric field for a thin single crystal of $\text{Lu}_{0.5}\text{Sc}_{0.5}\text{FeO}_3$, shown in the inset of Fig. 4(c). The observed $P(E)$ hysteresis loop confirms the existence of robust ferroelectricity at room temperature with a large coercive field of $\sim 100 \text{ kV}/\text{cm}$ and saturation polarization of $3.34(5) \mu\text{C}/\text{cm}^2$. This is slightly larger than the calculated polarization for this compound, denoted by the dashed line in the figure, however it is within error of that calculated for $\text{LuFe}_{1-x_{\text{Mn}}}\text{Mn}_{x_{\text{Mn}}}\text{O}_3$. This demonstrates that the atomic displacement method can be used to quantitatively predict the saturated polarization. The magnitude of the coercive field corroborates recent piezoelectric force microscopy measurements of thin films of LuFeO_3 where a similar field was found to induce complete sign reversal of the ferroelectric domains [16]. This also indicates good agreement between the domain energetics of both bulk and film materials.

C. Magnetic excitations and exchange interactions

Inelastic neutron-scattering measurements of the magnetic excitations in the form of spin waves provide a great deal of information about the underlying exchange interactions and local spin anisotropy. Shown in Fig. 5, these dynamics have been investigated in detail for the $x_{\text{Mn}} = 0.25$ compound. Constant energy transfer scans at $E = 6$ and 9 meV are shown in Figs. 5(a) and 5(b), respectively, while constant $Q = 1.3 \text{ \AA}^{-1}$ scans corresponding to the (101) magnetic reflection were also carried out and are shown in Figs. 5(c) and 5(d). The intensity of the scattering increases with increasing temperature as expected for the Boson population factor demonstrating that the scattering indeed originates from spin-wave excitations. At low temperature there is an abrupt increase in spectral weight above $E \sim 4 \text{ meV}$ indicative of a spin gap originating from single-ion anisotropy in the ordered state. The size of this gap is confirmed through high-resolution measurements on SPINS with an energy resolution of 0.25 meV , compared to the 1–2-meV resolution on BT-7.

We use a simple Hamiltonian, $H = -\sum_{\langle ij \rangle} J_{ij} S_i S_j + \sum_i D_z (S_i^z)^2$, for the exchange interactions along several important pathways to model the observed spin-wave density of states. This includes the superexchange interaction J_{nn} between nearest-neighbor moments within each plane, a much weaker interplane super-superexchange $\Delta J_c = J_{1c} - J_{2c}$, and a single-ion anisotropy term D_z along the c axis as indicated in Fig. 1(1). We constrained $\Delta J_c < 0$ (with $J_{2c} = 0$) to fix the magnetic ground state in the A_2 representation determined from our powder-diffraction measurements. A single in-plane interaction is sufficient here as the Fe ions are very close to the ideal position, meaning there should be very little difference between the six nearest-neighbor exchange interactions. A more complex Hamiltonian including further neighbor interactions and the Dzyaloshinskii-Moriya interaction could not be reliably studied given the polycrystalline nature of our sample and consequent measured density of states in lieu of direct dispersion relation data obtained on a single crystal. The spin-wave dispersion was calculated and then powder averaged using the SpinW package [33] and convoluted with

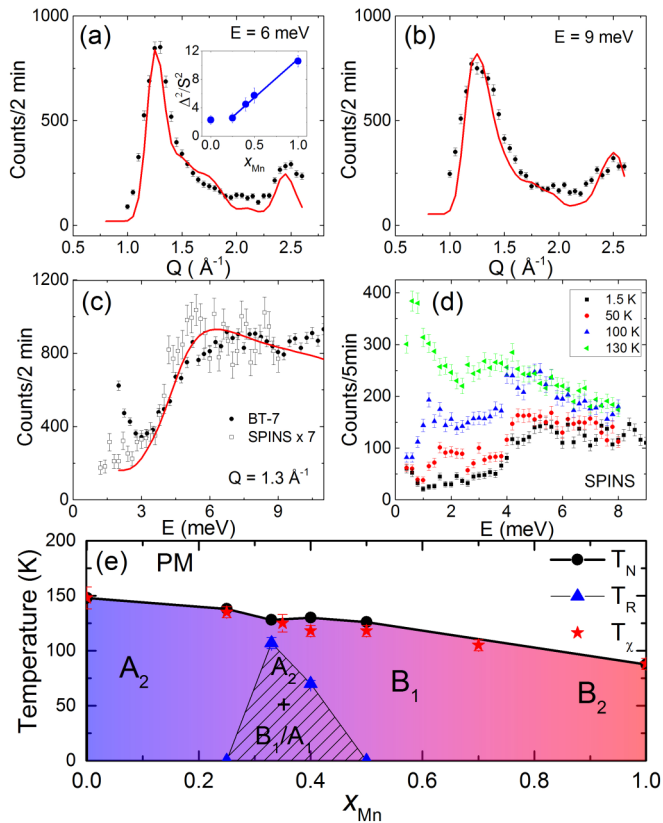


FIG. 5. (Color online) Inelastic neutron-scattering data at 3 K for constant energy transfer scans of $E = 6$ meV (a), 9 meV (b). The solid (black) circles are the data and the solid (red) curve is the model fit as described in the text. (c) Constant $Q = 1.3 \text{ \AA}^{-1}$ data taken on BT-7 and SPINS where the SPINS data have been scaled for comparison with the data taken on BT-7. The solid curve is the fit to the BT-7 data as in (a) and (b). (d) Temperature-dependent intensity for constant $Q = 1.3 \text{ \AA}^{-1}$ measured on SPINS. (e) Magnetic phase diagram determined from neutron scattering (T_N) and/or the derivative of the magnetic susceptibility (T_χ). T_N for $x_{\text{Mn}} = 0$ and 100 are taken from Refs. [16] and [23], respectively. The scaled spin gap as a function of x_{Mn} is shown in the inset in (a) where $x_{\text{Mn}} = 100$ is taken from Ref. [23] and $x_{\text{Mn}} = 0$ corresponds to Lu_{0.5}Sc_{0.5}FeO₃.

the instrument resolution function. The resulting spectrum is fit to the data in Figs. 5(a)–5(c) to extract the exchange and anisotropy parameters. A constant background and uniform scaling factor were also included as fitting parameters. The resulting best fit to this model, shown in Fig. 5 by the solid (red) curves, is given by $J_{\text{nn}} = -5.3(1)$ meV, $\Delta J_c = -0.05(2)$ meV, and $D_z = 0.06(2)$ meV.

The value of J_{nn} obtained for this composition is over 25% larger than that determined from single-crystal measurements of LuMnO₃ [23,24], and partly explains the observed increase in T_N found here. The interplane coupling ΔJ_c is of the same order as that previously noted in manganites, confirming the largely two-dimensional behavior of h -LuFeO₃ seen in similar layered structures [34,35]. We also find that the anisotropy parameter D_z is much smaller than for RMnO₃ compounds [23,24,35] consistent with the symmetric $3d^5$ high-spin Fe³⁺, and is indeed much closer to the value observed

in the orthoferrites such as YFeO₃ which contain isotropic Fe³⁺ spins [36].

Similar constant Q scans above the (101) magnetic reflection were performed for the remainder of the powder samples and Lu_{0.5}Sc_{0.5}FeO₃ to estimate the magnitude of the spin gap Δ for each compound. Calculations of the entire magnon dispersion show that Δ corresponds to the energy gap of a quartet of magnon bands that are nearly degenerate with minima at the Brillouin-zone center [23,24,34]. An analytical expression for Δ has been derived previously for a similar model Hamiltonian [34] and can be expressed in a simplified form here using only the exchange and average anisotropy interactions as $\frac{\Delta^2}{\langle S \rangle^2} \sim J_{\text{nn}} D_z$, where $\langle S \rangle$ is the average spin [28]. Shown in the inset of Fig. 5(e), $\frac{\Delta^2}{\langle S \rangle^2}$ decreases with decreasing Mn concentration, saturating below $x_{\text{Mn}} = 0.25$. From this it is apparent that D_z increases with x_{Mn} , as J_{nn} remains either constant or decreases somewhat following the observed concentration dependence of θ_{CW} as well as the values we extracted from fitting of the full powder-averaged dispersion.

These findings are summarized in the phase diagram shown in Fig. 5(e) as a function of temperature and x_{Mn} by combining the results from neutron scattering and susceptibility measurements along with previous results for end member compounds [15,16,23]. This clearly demonstrates that the transition temperature decreases linearly with x_{Mn} regardless of the ground-state magnetic structure. Construction of this phase diagram also implies that another spin-reorientation transition between purely antiferromagnetic structures exists in the Mn-rich region $0.5 < x_{\text{Mn}} < 1$ as the ground state of the $x_{\text{Mn}} = 0.5$ compound is distinct from LuMnO₃ [8,23,24].

D. Optimizing T_N in hexagonal $RM\text{O}_3$

We now compare these results with those of the other isostructural $RM\text{O}_3$ family compounds to establish more general structural dependences on the transition temperature, ground state, and routes to further enhance T_N . In Fig. 6 the T_N for several isostructural $RM\text{O}_3$ compounds are shown as a function of the ratio of the c/a lattice parameters [15,16,23,34,37]. Interestingly, we find a linear trend that is independent of both the R species as well as the transition metal (Fe or Mn). By extrapolating this trend, we estimate that $c/a > 2.15$ would be necessary to achieve room-temperature multiferroicity. To see how this may be achieved, we take the example of Lu_{0.5}Sc_{0.5}FeO₃ which currently has the highest T_N of any hexagonal multiferroic to date. At constant volume, the necessary c/a ratio could be achieved by reducing the in-plane lattice constant by 1.6% while simultaneously increasing c by 3.4%; this type of compressive strain is possible through epitaxial film growth by mismatching the lattice parameter of the substrate and film [38]. A simpler test of this principle could easily be made by mapping the dependence of T_N under uniaxial pressure or strain for these compounds.

A possible explanation for this systematic behavior can be found by examining the deformation of the oxygen hexahedra surrounding each M species, illustrated in Fig. 6. As the c/a ratio increases, we find that the oxygen hexahedra become elongated along the c axis, resulting in a lengthening the

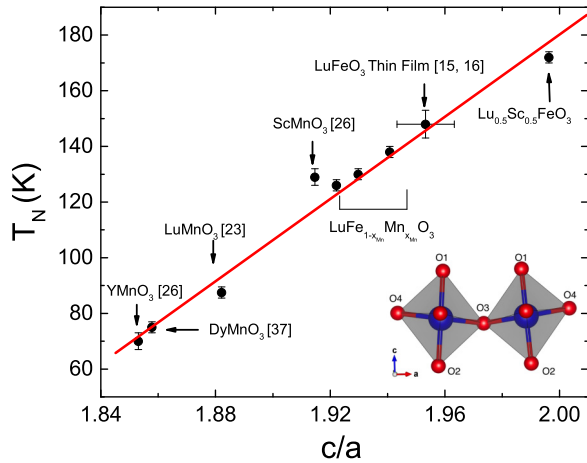


FIG. 6. (Color online) Néel transition temperatures as a function of lattice parameter for hexagonal $RM\text{O}_3$ ($R = \text{Lu}, \text{Dy}, \text{Sc}, \text{Y}$ and $M = \text{Mn}$ or Fe) taken from the literature. The solid (red) line is a linear fit through all of the data. Inset: Cartoon labeling the oxygen (red) positions defining the hexahedra surrounding the Mn or Fe species (blue).

O1-O2 bond and a reduction in the O3-O4 bond length and O1-O4-O3 bond angle [28]. Although the O1 and O2 oxygens do not participate in the primary exchange interaction resulting in magnetic order, the elongation of the hexahedra likely lowers the energy cost associated with filling the upper d_{z^2} orbital, thus stabilizing the $3d^5$ configuration of Fe^{3+} against decomposition to the orthorhombic structure observed in pure LuFeO_3 bulk materials [17]. Note that for a given M species, contraction of the a axis alone leads to reduced Fe-O-Fe distances, likely increasing the magnitude of J_{nn} resulting in an increase in T_N . Thus, by stabilizing the occupancy of the d_{z^2} orbital through this type of structural distortion we are able to simultaneously enhance the magnitude of the exchange interaction as well as average spin, both of which act to increase T_N while maintaining the ferroelectric structure. On the other hand, much of the interest in LuFeO_3 stems from the potential coupling between parallel ferromagnetic moments, which can

only occur for the A_2 representation. As we have shown here, however, the ground-state magnetic representation does not depend on the same lattice distortions as those which drive higher T_N and thus does not follow the general trend shown by T_N . Therefore, functional room-temperature multiferroic devices based on $P6_3cm$ structures will require independent control of both the unit-cell dimensions and relative distortion of the transition-metal position within the oxygen hexahedra. The former of these may be achievable using appropriate epitaxial techniques, while the latter may be tailored via transition-metal chemistry through doping.

IV. CONCLUSION

We have shown that the metastable hexagonal phase of LuFeO_3 can be stabilized in the bulk through either substitution of Mn onto the Fe site or Sc onto the Lu site. The magnetic ground state varies strongly as a function of composition, while for small Mn concentrations it is found to be identical to that found in $h\text{-LuFeO}_3$ films, including the appearance of a weak ferromagnetic moment as predicted by first-principle calculations [12]. Our measurements suggest that the Fe-rich phase is a strong candidate to realize the recently proposed magnetoelectric coupling and direct switching of the ferromagnetic moment via an electric field. Additionally, we have found that there is a strong connection between T_N and crystalline structure suggesting a possible route forward to achieving room-temperature multiferroicity in this material class.

ACKNOWLEDGMENTS

Work at Rutgers University was supported by the DOE under Grant No. DE-FG02-07ER46382, and work at Postech was supported by the Max Planck POSTECH/KOREA Research Initiative Program (Grant No. 2011-0031558) through NRF of Korea funded by MEST. S.M.D. acknowledges the support of a National Research Council NIST postdoctoral research associateship. We acknowledge useful conversations with H. Das and C. Fennie.

- [1] M. Gajek, M. Bibes, S. Fusil, K. Bouzehouane, J. Fontcuberta, A. Barthélémy, and A. Fert, *Nat. Mater.* **6**, 296 (2007).
- [2] J. F. Scott, *Nat. Mater.* **6**, 256 (2007).
- [3] R. O. Cherifi, V. Ivanovskaya, L. C. Phillips, A. Zobelli, I. C. Infante, E. Jacquet, V. Garcia, S. Fusil, P. R. Briddon, N. Guiblin, A. Mougin, A. A. Ünal, F. Kronast, S. Valencia, B. Dkhil, A. Barthélémy, and M. Bibes, *Nat. Mater.* **13**, 345 (2014).
- [4] S.-W. Cheong and M. Mostovoy, *Nat. Mater.* **6**, 14 (2007).
- [5] T. Choi, Y. Horibe, H. T. Yi, Y. J. Choi, Weida Wu, and S.-W. Cheong, *Nat. Mater.* **9**, 253 (2010).
- [6] D. B. Litvin, *Acta Crystallogr.* **A42**, 44 (1986).
- [7] J. Wang, J. B. Neaton, H. Zheng, V. Nagarajan, S. B. Ogale, B. Liu, D. Viehland, V. Vaithyanathan, D. G. Schlom, U. V. Waghmare, N. A. Spaldin, K. M. Rabe, M. Wuttig, and R. Ramesh, *Science* **299**, 1719 (2003).
- [8] T. Katsufuji, M. Masaki, A. Machida, M. Moritomo, K. Kato, E. Nishibori, M. Takata, M. Sakata, K. Ohoyama, K. Kitazawa, and H. Takagi, *Phys. Rev. B* **66**, 134434 (2002).
- [9] B. B. Van Aken, Thomas T. M. Palstra, A. Filippetti, and N. A. Spaldin, *Nat. Mater.* **3**, 164 (2004).
- [10] S. Artyukhin, K. T. Delaney, N. A. Spaldin, and M. Mostovoy, *Nat. Mater.* **13**, 42 (2014).
- [11] M. Fiebig, T. Lottermoser, and R. V. Pisarev, *J. Appl. Phys.* **93**, 8194 (2003).
- [12] H. Das, A. L. Wysocki, Y. Geng, W. Wu, and C. J. Fennie, *Nat. Commun.* **5**, 2998 (2014).
- [13] A. R. Akbashev, A. S. Semisalova, N. S. Perov, and A. R. Kaul, *Appl. Phys. Lett.* **99**, 122502 (2011).
- [14] W. Wang, J. Zhao, W. Wang, Z. Gai, N. Balke, M. Chi, H. N. Lee, W. Tian, L. Zhu, X. Cheng, D. J. Keavney, J. Yi, T. Z. Ward,

- P. C. Snijders, H. M. Christen, W. Wu, J. Shen, and X. Xu, *Phys. Rev. Lett.* **110**, 237601 (2013).
- [15] J. A. Moyer, R. Misra, J. A. Mundy, C. M. Brooks, J. T. Heron, D. A. Muller, D. G. Schlom, and P. Schiffer, *APL Mater.* **2**, 012106 (2014).
- [16] S. M. Disseler, J. A. Borchers, C. M. Brooks, J. A. Mundy, J. A. Moyer, D. A. Hillsberry, E. L. Thies, D. A. Tenne, J. Heron, M. E. Holtz, J. D. Clarkson, G. M. Stiehl, P. Schiffer, D. A. Muller, D. G. Schlom, and W. D. Ratcliff, *Phys. Rev. Lett.* **114**, 217602 (2015).
- [17] R. L. White, *J. Appl. Phys.* **40**, 1061 (1964).
- [18] A. Masuno, A. Ishimoto, C. Moriyoshi, N. Hayashi, H. Kawaji, Y. Kuroiwa, and H. Inoue, *Inorg. Chem.* **52**, 11889 (2013).
- [19] J. Rodriguez-Cavajal, *Physica B* **192**, 55 (1993).
- [20] J. W. Lynn, Y. Chen, S. Chang, Y. Zhao, S. Chi, W. Ratcliff II, B. G. Ueland, and R. W. Erwin, *J. Res. NIST* **117**, 61 (2012).
- [21] S. Lee, A. Pirogov, M. Kang, K.-H. Jang, M. Yonemura, T. Kamiyama, S.-W. Cheong, F. Gozzo, N. Shin, H. Kimura, Y. Noda, and J.-G. Park, *Nature (London)* **451**, 805 (2008).
- [22] P. Tong, D. Louca, N. Lee, and S.-W. Cheong, *Phys. Rev. B* **86**, 094419 (2012).
- [23] H. J. Lewtas, A. T. Boothroyd, M. Rotter, D. Prabhakaran, H. Müller, M. D. Le, B. Roessli, J. Gavilano, and P. Bourges, *Phys. Rev. B* **82**, 184420 (2010).
- [24] J. Oh, M. D. Le, J. Jeong, J.-h. Lee, H. Woo, W.-Y. Song, T. G. Perring, W. J. L. Buyers, S.-W. Cheong, and J.-G. Park, *Phys. Rev. Lett.* **111**, 257202 (2013).
- [25] Y. Ren, T. T. M. Palstra, D. I. Khomskii, E. Pellegrin, A. A. Nugroho, A. A. Menovsky, and G. A. Sawatzky, *Nature (London)* **396**, 441 (1998).
- [26] A. Muñoz, J. A. Alonso, M. J. Martínez-Lope, M. T. Casáis, J. T. Martínez, and M. T. Fernández-Díaz, *Phys. Rev. B* **62**, 9498 (2000).
- [27] P. J. Brown and T. Chatterji, *J. Phys.: Condens. Matter* **18**, 10085 (2006).
- [28] See Supplemental Material at <http://link.aps.org/supplemental/10.1103/PhysRevB.92.054435> for additional information regarding details of experimental parameters as well as crystallographic analysis with listings of atomic positions, etc.
- [29] O. V. Kovalev, *Sov. Phys. Solid State* **5**, 2309 (1964).
- [30] X. Fabrèges, S. Petit, I. Mirebeau, S. Pailhès, L. Pinsard, A. Forget, M. T. Fernandez-Diaz, and F. Porcher, *Phys. Rev. Lett.* **103**, 067204 (2009).
- [31] H. Wang, I. V. Solovyev, W. Wang, X. Wang, P. J. Ryan, D. J. Keavney, J.-W. Kim, T. Z. Ward, L. Zhu, J. Shen, X. M. Cheng, L. He, X. Xu, and X. Wu, *Phys. Rev. B* **90**, 014436 (2014).
- [32] J. M. Perez-Mato, D. Orobengoa, and M. I. Aroyo, *Acta Crystallogr., Sect. A* **66**, 558 (2010).
- [33] S. Toth and B. Lake, *J. Phys.: Condens. Matter* **27**, 166002 (2015).
- [34] T. J. Sato, S.-H. Lee, T. Katsufuji, M. Masaki, S. Park, J. R. D. Copley, and H. Takagi, *Phys. Rev. B* **68**, 014432 (2003).
- [35] O. P. Vajk, M. Kenzelmann, J. W. Lynn, S. B. Kim, and S.-W. Cheong, *Phys. Rev. Lett.* **94**, 087601 (2005).
- [36] S. E. Hahn, A. A. Podlesnyak, G. Ehlers, G. E. Granroth, R. S. Fishman, A. I. Kolesnikov, E. Pomjakushina, and K. Conder, *Phys. Rev. B* **89**, 014420 (2014).
- [37] J. S. Helton, D. K. Singh, H. S. Nair, and S. Elizabeth, *Phys. Rev. B* **84**, 064434 (2011).
- [38] A. Bhattachaya and S. May, *Annu. Rev. Mater. Res.* **44**, 65 (2014).